This article has been accepted for publication in a future issue of this journal, but has not been fully edited. Content may change prior to final publication. Citation information: DOI 10.1109/TII.2019.2903893, IEEE Transactions on Industrial Informatics

A Robotic Cane for Balance Maintenance Assistance

***Abstract*—This paper proposes a robotic cane that helps users to stand and maintain their balance while standing and walking. The design is based on an inverted pendulum model, uses a smart omnidirectional wheel, and is linearized by the Lie algebra method (LAM) combined with a nonlinear disturbance observer that estimates the external force applied by the user. The hardware and mathematical model of the robotic cane are analyzed in detail. The hardware design is complete, and considers the weight and battery capacity. The performance of the controller is confirmed in 3D simulations and in physical experiments. The robotic cane tolerates a large fluctuation angle from its equilibrium point. It also has a fall prevention function, which is among the most desirable functions of any walking assistance device, and responds quickly to a human force. The balance maintenance functions are as follows: self-balance, standing and walking assistance, fall prevention, and a mechatronic safety mode. In experimental measurements of the cane in use, the gyroscope sensor insignificant vibrations on the user's bodies, verifying the effectiveness of the robotic cane in daily life activities. The performance of LAM is also compared with that of the linear quadratic regulator (LQR).**

***Index Terms*—Robotic cane, inverted pendulum, omnidirectional wheel, walking assistance, Lie algebra method.**

I. Introduction

Populations are aging dramatically. Especially in developed countries, where the estimated number of people aged 65 or older has escalated from 524 million in 2010 to nearly 1.5 billion in 2050 [1], health care for elderly and disabled people has become a serious problem. Walking assistance robots will play an important role in these problems.

Wearable robots [2]–[9] support walking and movement, but are quite complicated and must be worn on the leg joints, which is uncomfortable for the user and risks entanglement in the apparatuses. Therefore, they are suitable only in designated rehabilitation centers, and are ineffective in daily living activities.

Another type of mobility assistance robot is the smart wheelchair [10], [11], which is mounted on four wheels and supports users on the seat. Although these wheelchairs are suitable for elderly and disable users, they are cumbersome and require a large working or maneuvering space. They may also require an additional person to operate them. Thus, smart wheelchairs are limited to home use or to rehabilitation centers where additional helpers are available.

More flexible assistance robots have been proposed in [12], [13]. Users of these robots walk while gripping the robot. However, like wheelchair robots, these robots are bulky, need a large maneuvering space, and may require additional operators. Moreover, their use is limited to flat surfaces.

The authors [14] controlled the position of a robotic cane using three omnidirectional wheels. Besides turning easily, their robotic cane has a fall prevention functionality which is indispensable for walking assistance devices, but the hardware design remains bulky and complicated.

Following this first application of omnidirectional wheels to a robotic cane controlled by dedicated hardware [14], researchers developed robotic canes with a single omnidirectional wheel [15]–[18]. However, their approaches were tested in simulation studies rather than on real products for practical applications. Especially, the authors of [19] filed a patent for their robotic cane design without experimental verification. The single omnidirectional wheel is more compact than the omnidirectional ball robot [20] or the three Omni-wheeled cane robot [14], and significantly reduces the size of the robotic cane. Minimizing the size is important for any assist device.

This paper proposes a robotic cane that helps users to maintain their balance, while overcoming the disadvantages of the earlier designs. The robotic cane uses a specially designed smart omnidirectional wheel, conferring both compactness and flexibility. The design is based on inverted pendulum theory and is linearized by the Lie algebra method (LAM). The human force on the robotic cane is estimated by a nonlinear disturbance observer.

To achieve our target, we adopt a popular mechanical system (the inverted pendulum), as our basic model. In previous studies, the stability of the inverted pendulum was controlled by various method: fuzzy-logic [21], [22]; basic control loop feedback [23]; a linear quadratic regulator (LQR) [24], [25]; Newton networks [26], [27]; additional sliding-mode control [28], [29], and a nonlinear disturbance observer [30]. Improving stability increases the performance of the controller output. The authors of [31], [32] controlled the velocity and position of a traditional inverted pendulum model by two new controllers. The installed controllers strongly and stably maintained the robot's position at the desired point in simulations, but their performance was not tested in physical experiments. The authors [33] controlled the torque and velocity of wheeled inverted pendulum motors in an analytical simulation study, and described the trade-offs between the control methodologies in different application situations.

However, the inverted pendulums in the above studies were stable only around the equilibrium point. Such a small stability range is unsuitable for walking assistance devices in general, and robotic canes in particular. To maintain the user's balance, all walking assistance devices must stable far from the equilibrium position. The present paper resolves the equilibrium problem through the LAM and the nonlinear disturbance observer. The LAM is simply applied to the controller and

This article has been accepted for publication in a future issue of this journal, but has not been fully edited. Content may change prior to final publication. Citation information: DOI 10.1109/TII.2019.2903893, IEEE Transactions on Industrial Informatics

linearizes the robotic cane even when the fluctuation angle largely deviates from equilibrium. Meanwhile, the nonlinear disturbance observer calculates the human force applied to the robotic cane. Consequently, the robotic cane is equipped with a fall prevention functionality, a highly desirable property of any walking assistance device.

Another main contribution is the complete hardware design. Especially, the controller is designed with high accuracy, high speed, and optimized parameters. We experimentally demonstrate the strong stable standing and response of the robot to user behavior. The robotic cane effectively helps users to maintain their balance. Moreover, the LAM is more stable in self-standing mode than the LQR method, which generates some vibrations. In particular, if users begin to fall backward or forward, the robotic cane quickly restores their equilibrium centers, we received much positive feedback from elderly and disabled participants. The robotic cane also passed the electromagnetic compatibility test, confirming its safety near human bodies.

The remainder of this paper is organized as follow: Section II, details the hardware of the robotic cane, and Section III obtains the controller parameters by solving the mathematical equations of the robotic cane (the LAM and the nonlinear disturbance observer). The controller is then designed with high processing speed and accuracy. Section IV demonstrates the performance of the controller in simulations and experimental tests. The body vibration is estimated by a sensor gyroscope attached to the user. The performance of the nonlinear disturbance observer is also compared with that of LQR. Conclusions and future works are summarized in Section V.

II. Hardware of the Robotic Cane

This section presents the hardware details of the robotic cane.

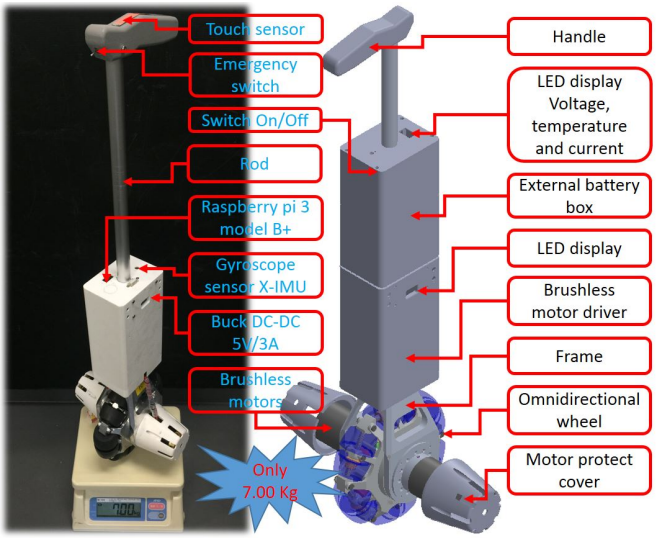

Fig. 1. Hardware of the designed robotic cane.

As shown in Fig. 1, our robotic cane includes a grip handle, a rod, and a balance control sensor. It has a LED display that reports the temperature, voltage, and current of the external battery box, an on/off power switch, and an emergency switch. The working modes of the robotic cane can be controlled and changed by a touch sensor, and another LED displays the voltage of the battery inside the cane's main body. The position of the robotic cane is controlled by two brushless motors driven by two motor drivers, and an encoder. The brushless motors are protected by plastic covers made by a 3D printer. The frame connects the main body to the omnidirectional wheel. The angle and velocity of the rod are calculated by a small Raspberry Pi 3 Model B+ computer inside the main body. The computer is connected to an X-IMU gyroscope sensor, and is powered through a 5V/3A step-down converter.

The balancing velocity, which maintains the upright position of the cane, is calculated from the speed and direction of the motorized omnidirectional wheel.

The balancing velocity is calculated from the speed and direction of the motorized omnidirectional wheel required to keep the robotic cane in a substantially upright position. Depending on the control signal sent from the controller, the algorithm of the robotic cane either maintains stability around the equilibrium value or supports the balance maintenance of the user.

Owing to the special structure of the gearbox and omnidirectional wheel (see Fig. 2), the robotic cane can move to the left or right on the lateral wheels, or backward or forward on the sagittal wheel, achieving an omnidirectional response to the speed and rotation direction of the two brushless motors. Fig. 3 shows the internal structure of the gearbox, consisting of bevel gears and a harmonic gear.

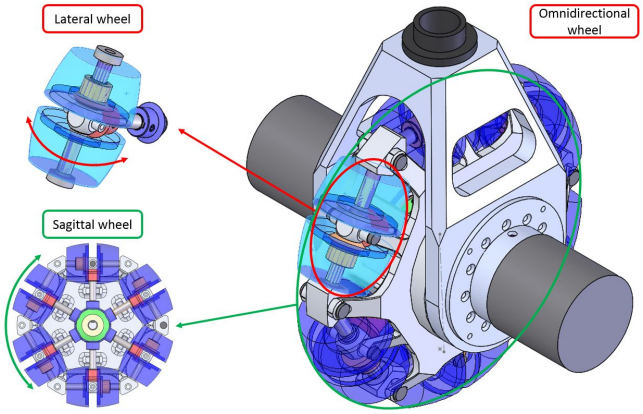

Fig. 2. Structure of the gearbox with lateral and sagittal wheels.

Fig. 4 shows the operational principle of the gearbox. Opposite rotation directions of the two brushless motors elicit left-right movements of the lateral wheels. Conversely, when the two motors rotate in the same direction, the sagittal wheel turns around the motor axis. In this way, we can steer the robotic cane in any direction depending on the speed and rotation directions of the two brushless motors.

Moreover, the encoders on the motor axis read the real speed of the robotic cane enabling precise control of the cane's motion.

The parameters of harmonic gear are given in Table I. The harmonic gear is compact and lightweight, with high torque

This article has been accepted for publication in a future issue of this journal, but has not been fully edited. Content may change prior to final publication. Citation information: DOI 10.1109/TII.2019.2903893, IEEE Transactions on Industrial Informatics

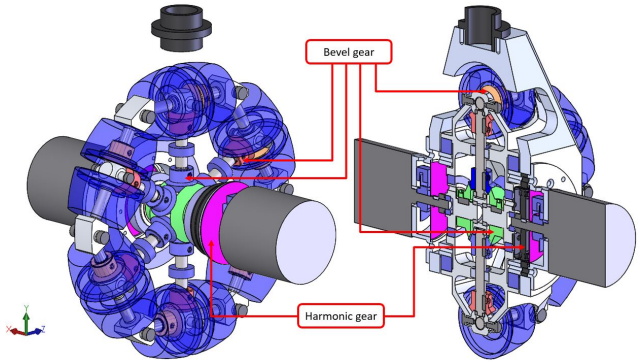

Fig. 3. Internal structure of the gearbox by using bevel gears and a harmonic gear.

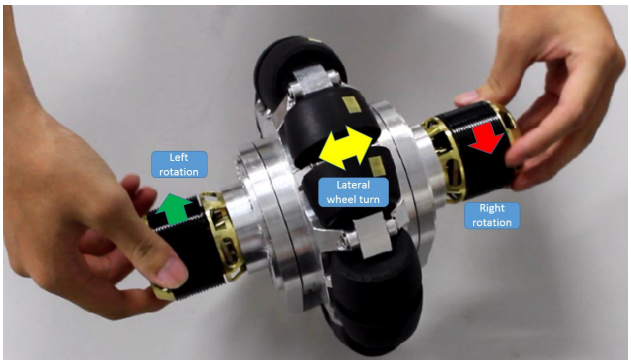

Fig. 4. Operation of the gearbox depending on the speed and rotation of the two brushless motors.

capability of the sagittal wheel. For balance maintenance during standing or walking, the robotic cane determines the output torque from the two motors.

TABLE I
PARAMETERS OF THE HARMONIC GEAR (CSD-20-50-2A-GR-SP)

Explanation	Value	Unit
Reduction ratio	50	
Allowable peak torque of the start and stop time	39	Nm
Maximum allowable value of the average load torque	24	Nm
Maximum allowable momentary torque	69	Nm
Maximum allowable input rotational speed	6500	rpm
Average allowable input rotational speed	3500	rpm

The rod angle ϕ (Fig. 6) of the robotic cane when moving or standing is detected by the gyroscope sensor and an accelerometer. To control the balance maintenance, the user's applied force is determined from the velocity of the robotic cane. Meanwhile, the brushless motors are controlled by two DC motor drivers (Table II) based on motion control technology. The speed and torque of the brushless motors (Table III) were selected to maximize their efficiency while ensuring easy and perfect operation by users.

These motor drivers are controlled by the motion signals received from the central controller. The control signals depend on the designed algorithm. The completed hardware of the robotic cane, including the batteries, weighs 7.0 Kg (see Fig. 1). When the robotic cane is expected to operate for over one hour without charging, it is equipped with an outer battery of approximate mass 2.3 kg (25.2V, 13.8 Ah).

TABLE II
PARAMETERS OF THE MOTOR DRIVER (ELMO MOTION CONTROL G-DCWHI20/100EE)

Explanation	Value	Unit
Minimum DC supply voltage	12	V
Nominal DC supply voltage	85	V
Maximum DC supply voltage	95	V
Maximum continuous power output	1600	W
Amplitude sinusoidal/DC continuous current	20	A
Sinusoidal continuous RMS current limit	14.1	A
Peak current limit	28.2	A

TABLE III
PARAMETERS OF THE BRUSHLESS MOTORS (HK-4525-520KV)

Explanation	Value	Unit
Stator diameter	45	mm
Stator thickness	25	mm
Motor Kv	520KV	rpm/V
Max continuous Current	100	A
Max continuous Power	4450	W
Weight	470	gram
Outside diameter	56.7	mm
Shaft diameter	5.98	mm
Body length	53.4	mm
Overall shaft length	91.5	mm
Max peak current (2 sec)	230	A
Max peak power (2 sec)	10.2	kW
Pole pairs	5	

Fig. 5 is a block diagram of the robotic cane system.

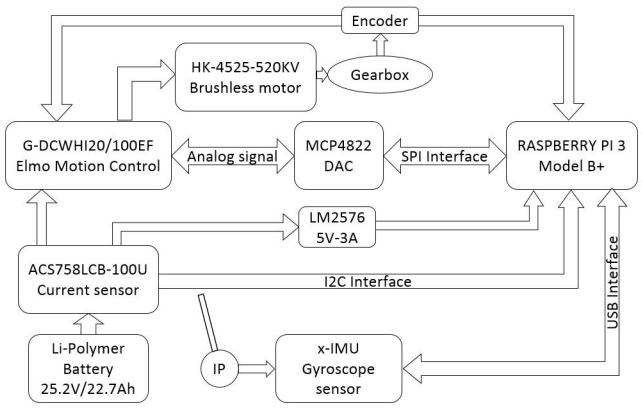

Fig. 5. Block diagram of the robotic cane system.

The central controller is a Raspberry Pi 3 Model B+ with a serial peripheral interface connected to a digital-to-analog converter circuit. An Inter-Integrated Circuit (I2C) interface is connected to the ADC circuit. To control the robotic cane operation, a USB interface is linked to the X-IMU gyroscope sensor module (Table IV).

TABLE IV
PARAMETERS OF THE GYROSCOPE SENSOR MODULE (X-IMU)

Explanation	Value	Unit
Power supply voltage	3.3 to 6.3	V
Dimensions	33x42x10	mm
Weight	12	gram
Gyroscope range	±2000	degree/s
Accelerometer range	±8	g

III. MATHEMATICAL MODEL AND DESIGN OF THE CONTROLLER SYSTEM OF THE ROBOTIC CANE

A. Mathematical model of the robotic cane based on the inverted pendulum model

The rotation angles of the omnidirectional wheel are related to the rotation angles of the two motors as described in (1) and (2):

$$\theta_{Pitch} = G_H \frac{\theta_R + \theta_L}{2} \tag{1}$$

$$\theta_{Roll} = G_B G_H \frac{\theta_R - \theta_L}{2} \tag{2}$$

where θ_{Pitch}, θ_{Roll}, θ_R, and θ_L denote the angles of the major wheel, minor wheel, left motor and right motor respectively, and G_H and G_B are the gear reduction ratios of the harmonic and bevel gears respectively, with G_H = 1/50 (Table I) and G_B = 2.

From (1) and (2), the wheel torques that control the inverted pendulum in the sagittal and lateral planes are distributed to the motor torques and control are seamlessly controlled by Eqs. (3) and (4).

$$\tau_R = \frac{1}{G_H}\tau_{Pitch} + \frac{1}{G_B G_H}\tau_{Roll} \tag{3}$$

$$\tau_L = \frac{1}{G_H}\tau_{Pitch} - \frac{1}{G_B G_H}\tau_{Roll} \tag{4}$$

The standard coordinate system is shown in Fig. 6. The system has two basic planes: a sagittal plane ($x - z$), and a lateral plane ($y - z$). In the sagittal and lateral planes, the robotic cane can be regarded as an inverted pendulum with one large wheel and small wheels, respectively. The torques of the left and right motors calculated by (1) and (2), respectively, are identical in the sagittal and lateral planes but differ in their input parameters.

The symbols used in these equations are defined in Table V and the equations of motion are:

$$\frac{d}{dt}\left(\frac{\partial L}{\partial \dot{\phi}}\right) - \frac{\partial L}{\partial \phi} + \frac{\partial F_{fr}}{\partial \dot{\phi}} = 0 - d_1 \tag{5}$$

$$\frac{d}{dt}\left(\frac{\partial L}{\partial \dot{\theta}}\right) - \frac{\partial L}{\partial \theta} + \frac{\partial F_{fr}}{\partial \dot{\theta}} = \tau - d_2 \tag{6}$$

where L is the Lagrangian and the other symbols are used in (7)-(14):

$$L = T - V \tag{7}$$

$$F_{fr} = \frac{1}{2}D_\phi \dot{\phi}^2 + \frac{1}{2}D_\theta \dot{\theta}^2 \tag{8}$$

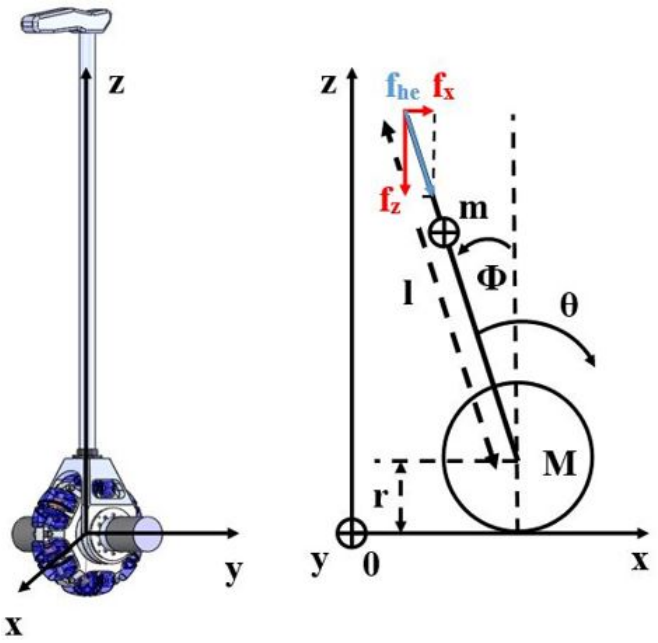

Fig. 6. Coordinate system of the robotic cane based on the inverted-pendulum model.

TABLE V
EXPLANATION OF SYMBOLS

Explanation	Symbol	Unit
Rotational kinetic energy of wheel	T_1	J
Rotational kinetic energy of rod	T_2	J
Translational kinetic energy of wheel	T_3	J
Translational kinetic energy of rod	T_4	J
Kinetic energy total	T	J
Potential energy total	V	J
Inertia of rod	J_ϕ	kg·m^2
Inertia of wheel	J_θ	kg·m^2
Viscous friction coefficient of rod	D_ϕ	N.m.s/rad
Viscous friction coefficient of wheel	D_θ	N.m.s/rad
Length of rod	l	m
Center of mass of rod	l_c	m
Mass of rod	m	kg
Mass of wheel	M	kg
Actuation torque	τ	N.m
Actuation torque on the right motor	τ_R	N.m
Actuation torque on the left motor	τ_L	N.m
Gravitational acceleration	g	m/s^2
Radius of wheel	r	m
Angle of the rod	ϕ	rad
Angle of the wheel	θ	rad
Disturbance according to ϕ	d_1	Nm
Disturbance according to θ	d_2	Nm

$$T_1 = \frac{1}{2}J_\theta(\dot{\theta} - \dot{\phi})^2 \tag{9}$$

$$T_2 = \frac{1}{2}J_\phi \dot{\phi}^2 \tag{10}$$

$$T_3 = \frac{1}{2}Mr^2(\dot{\theta} - \dot{\phi})^2 \tag{11}$$

$$T_4 = \frac{1}{2}m([\frac{d}{dt}(r(\theta - \phi) - l\sin\phi)]^2 + [\frac{d}{dt}(l\cos\phi)]^2) \tag{12}$$

$$T = \sum_{i=1}^{4} T_i \tag{13}$$

$$V = mgl\cos\phi \tag{14}$$

The transfer function matrix of the inverted pendulum for analyzing the robotic cane's motion is computed as:

$$\begin{bmatrix} H_{11} & H_{12} \\ H_{21} & H_{22} \end{bmatrix} \begin{bmatrix} \ddot{\phi} \\ \ddot{\theta} \end{bmatrix} + \begin{bmatrix} b_1 \\ b_2 \end{bmatrix} = \begin{bmatrix} -d_1 \\ \tau - d_2 \end{bmatrix} \tag{15}$$

The elements of this equation are given by (16)-(20):

$$H_{11} = J_\theta + (M+m)\,r^2 + 2mrl\cos\phi + J_\phi + ml^2 \tag{16}$$
$$H_{12} = H_{21} = -J_\theta - (M+m)\,r^2 - mrl\cos\phi \tag{17}$$
$$H_{22} = J_\theta + (M+m)\,r^2 \tag{18}$$
$$b_1 = -\dot{\phi}^2 mrl\sin\phi - mgl\sin\phi + D_\phi\dot{\phi} \tag{19}$$
$$b_2 = \dot{\phi}^2 mrl\sin\phi + D_\theta\dot{\theta} \tag{20}$$

The torque output to the motor axis, which guides the movement of the robotic cane, is given by:

$$\tau = (H_{22} - \frac{H_{12}H_{21}}{H_{11}})u - \frac{H_{21}}{H_{11}}b_1 - \frac{H_{21}}{H_{11}}d_1 + b_2 + d_2 \tag{21}$$

B. LAM linearization of the nonlinear system

When recast in the form of (22), the motion equations (15) of the robotic cane are easily recognized as a nonlinear system.

$$\dot{x} = \begin{bmatrix} \dot{\phi} \\ \ddot{\phi} \\ \dot{\theta} \\ \ddot{\theta} \end{bmatrix} = \begin{bmatrix} \dot{\phi} \\ -\frac{b_1}{H_{11}} - \frac{d_1}{H_{11}} \\ \dot{\theta} \\ 0 \end{bmatrix} + \begin{bmatrix} 0 \\ -\frac{H_{12}}{H_{11}} \\ 0 \\ 1 \end{bmatrix} u \tag{22}$$

Defining the following functions the nonlinear system is linearized by the following LAM expression.

$$\dot{x} = f(x) + g(x)u \tag{23}$$
$$y = h(x) \tag{24}$$

$$L_f h(x) = \sum_{i=1}^{n} \frac{\partial h}{\partial x_i} f_i(x) = \frac{\partial h}{\partial x}(x) f(x) \tag{25}$$

The derivative of y by t is expanded as follows:

$$\frac{dy}{dt} = \frac{\partial h}{\partial x}\frac{\partial x}{dt} = \frac{\partial h}{\partial x}(f(x) + g(x)u) = L_f h(x) + L_g h(x)u \tag{26}$$

Combining this expression with the following law (27) [34], with $r < n$:

$$\begin{cases} L_g {L_f}^{(r-1)} h \neq 0 \\ L_g h = L_g L_f h = L_g {L_f}^2 h = \ldots = L_g {L_f}^{(r-2)} h = 0 \end{cases} \tag{27}$$

We have the expanded the equations of y by t as shown in (28)-(30):

$$\dot{y} = L_f h \tag{28}$$
$$\ddot{y} = {L_f}^2 h \tag{29}$$
$$\vdots$$
$$y^{(r)} = {L_f}^r h(x) + L_g {L_f}^{(r-1)} h(x) u \tag{30}$$

where the input value of the controller is calculated by:

$$u = \frac{v - {L_f}^r h(x)}{L_g {L_f}^{(r-1)} h(x)} \tag{31}$$

We define y as a function of ϕ and θ in (32). Hence, the derivatives of y with respect to t are calculated by (33) and (34) as follows:

$$y = \sigma_1(\phi) + \sigma_2(\theta) \tag{32}$$
$$\dot{y} = \frac{\partial \sigma_1(\phi)}{\partial \phi}\dot{\phi} + \frac{\partial \sigma_2(\theta)}{\partial \theta}\dot{\theta} \tag{33}$$
$$\ddot{y} = \frac{\partial^2 \sigma_1(\phi)}{\partial \phi^2}\dot{\phi}^2 + \frac{\partial^2 \sigma_2(\theta)}{\partial \theta^2}\dot{\theta}^2 - \frac{b1}{H_{11}}\frac{\partial \sigma_2(\theta)}{\partial \theta} + (\frac{H_{12}}{H_{11}}\frac{\partial \sigma_1(\phi)}{\partial \phi} - \frac{\partial \sigma_2(\theta)}{\partial \theta})u \tag{34}$$

Comparing (34) with the law in (27), we have:

$$\frac{H_{12}}{H_{11}}\frac{\partial \sigma_1(\phi)}{\partial \phi} - \frac{\partial \sigma_2(\theta)}{\partial \theta} = 0 \tag{35}$$

From (35), we can find the elements of (32) as follows:

$$\frac{\partial \sigma_1(\phi)}{\partial \phi} = \frac{H_{11}}{H_{12}} \tag{36}$$
$$\frac{\partial \sigma_2(\theta)}{\partial \theta} = 1 \tag{37}$$

Thus, (32) is redefined as follows:

$$y = \int_0^\phi \frac{H_{11}}{H_{12}} d\phi + \theta \tag{38}$$

Similarly, the derivatives of the new variable y are calculated by (39)-(42). These equations are the linearized equations of the nonlinear system of the inverted pendulum:

$$y = \int_0^\phi \frac{H_{11}}{H_{12}} d\phi + \theta \tag{39}$$
$$\dot{y} = \frac{H_{11}}{H_{12}}\dot{\phi} + \dot{\theta} \tag{40}$$
$$\ddot{y} = \frac{\partial}{\partial \phi}\frac{H_{11}}{H_{12}}\dot{\phi}^2 - \frac{b_1}{H_{12}} \tag{41}$$
$$y^{(3)} \simeq \frac{\partial^2}{\partial \phi^2}\frac{H_{11}}{H_{12}}\dot{\phi}^3 - \frac{\partial}{\partial \phi}\frac{b_1}{H_{12}}\dot{\phi} - 2(\frac{\partial}{\partial \phi}\frac{H_{11}}{H_{12}})\frac{b_1}{H_{11}}\dot{\phi} \tag{42}$$

To simplify the analysis and programming (the relatively simple equations are easily computed by the microcontroller with a short control sampling time), we use the expansion (31) with the derivative rank $r = 4$. Thus, the input value is given by:

$$u = \frac{v - {L_f}^4 h(x)}{L_g {L_f}^3 h(x)} \tag{43}$$

This article has been accepted for publication in a future issue of this journal, but has not been fully edited. Content may change prior to final publication. Citation information: DOI 10.1109/TII.2019.2903893, IEEE Transactions on Industrial Informatics

The parameters in (31) are similar to those in (44)-(45):

$$L_g L_f{}^3 h(x) = -3\frac{\partial^2}{\partial\phi^2}\frac{H_{11}}{H_{12}}\frac{H_{12}}{H_{11}}\dot{\phi}^2 + \frac{\partial}{\partial\phi}\frac{b_1}{H_{12}}\frac{H_{12}}{H_{11}} + 2\frac{\partial}{\partial\phi}\frac{H_{11}}{H_{12}}\frac{H_{12}}{H_{11}{}^2}b_1 \tag{44}$$

$$L_f{}^4 h(x) = -\frac{\partial^2}{\partial\phi^2}\frac{b_1}{H_{12}}\dot{\phi}^2 + \frac{\partial^3}{\partial\phi^3}\frac{H_{11}}{H_{12}}\dot{\phi}^4 - 5(\frac{\partial^2}{\partial\phi^2}\frac{H_{11}}{H_{12}})\frac{b_1}{H_{11}}\dot{\phi}^2 - 2\frac{\partial}{\partial\phi}\frac{b_1}{H_{12}}\dot{\phi}^2 + \frac{\partial}{\partial\phi}\frac{b_1}{H_{12}}\frac{b_1}{H_{11}} + 2\frac{\partial}{\partial\phi}\frac{H_{11}}{H_{12}}\left(\frac{b_1}{H_{11}}\right)^2 \tag{45}$$

Thus, the controller coefficient is defined as:

$$v = -\sum_{i=0}^{3}\lambda_i(y^{(i)} - y_{ref}^{(i)}) \tag{46}$$

C. Nonlinear disturbance observer

The general motion equation of the robotic cane is rewritten as follows:

$$\frac{\mathrm{d}}{\mathrm{dt}}\left(\frac{\partial \mathrm{L}}{\partial\dot{q}}\right) - \frac{\partial \mathrm{L}}{\partial q} = \tau_{all} - d \tag{47}$$

where, d is the generalized load torque applied by the user.

The state space of the nonlinear disturbance observer [18] is represented by:

$$\dot{\xi} = -K\xi + K^2\frac{\partial L}{\partial\dot{q}} + K(\frac{\partial L}{\partial q} + \tau_{all}) \tag{48}$$

$$\hat{d} = \xi - K\frac{\partial L}{\partial\dot{q}} \tag{49}$$

where $\hat{d}$ is the estimated disturbance, ξ is the observer state variable, L is the Lagrangian, and K is the gain of the observer.

The human force f_{he} in the coordinate system of Fig. 6 is divided into a vertical component f_z and a horizontal component f_x (or f_y). These two forces, denoted as d_1 and d_2, respectively, are respectively given by.

$$d_1 = (-l_c\cos\phi - r)f_x - l_c\sin\phi f_z \tag{50}$$

$$d_2 = rf_x \tag{51}$$

The forces applied on the robotic cane by the user, and during movement of the cane by the user, are not measured by a human force sensor. Translational (x-or y-directional) motion of the robot is liked to the axial rotation of the robot, while the vertical (z-direction) relates to the rod movement of the robot. The force exerted by the user is obtained from the nonlinear disturbance observer as follows (see also Fig. 8).

$$\hat{f}_x = \frac{\hat{d}_2}{r} \tag{52}$$

$$\hat{f}_z = -\frac{1}{l_c r\sin\phi}\left\{(l_c\cos\phi + r)\hat{d}_2 + r\hat{d}_1\right\} \tag{53}$$

The angle reference of the rod ϕ_{ref} is calculated from the disturbance force $\hat{d}_1$ as:

$$\phi_{ref} = \sin^{-1}\frac{\hat{d}_1}{l_c mg} \tag{54}$$

The wheel angle reference, defining the required distance to move from the current angle rod $\phi_{current}$ to the reference rod angle, is determined as:

$$\theta_{ref} = \frac{l_c\sin\phi_{ref}}{r} \tag{55}$$

The wheel angular velocity is simply proportional to the integral of the human force applied to the rod of the robotic cane d_2, the external torque that tries to rotate the wheel.

$$\dot{\theta}_{ref} = K_I\int\frac{\hat{d}_2}{r}dt \tag{56}$$

where K_I is the integral gain.

In terms of the reference parameters, the controller equations are recast as:

$$y_r = \int_0^{\phi_r}\frac{H_{11}}{H_{12}}d\phi_r + \theta_r \tag{57}$$

$$\dot{y}_r = \frac{H_{11}}{H_{12}}\dot{\phi}_r + \dot{\theta}_r \tag{58}$$

$$\ddot{y}_r = \frac{\partial}{\partial\phi_r}\frac{H_{11}}{H_{12}}\dot{\phi}_r^2 - \frac{b_1}{H_{12}} \tag{59}$$

$$y_r{}^{(3)} \simeq \frac{\partial^2}{\partial{\phi_r}^2}\frac{H_{11}}{H_{12}}\dot{\phi}_r^3 - \frac{\partial}{\partial\phi_r}\frac{b_1}{H_{12}}\dot{\phi}_r - 2(\frac{\partial}{\partial\phi_r}\frac{H_{11}}{H_{12}})\frac{b_1}{H_{11}}\dot{\phi}_r \tag{60}$$

and, the coefficients of their equations as (61) - (65):

$$H_{11} = J_\theta + (M+m)r^2 + 2mrl\cos\phi_r + J_\phi + ml^2 \tag{61}$$

$$H_{12} = H_{21} = -J_\theta - (M+m)r^2 - mrl\cos\phi_r \tag{62}$$

$$H_{22} = J_\theta + (M+m)r^2 \tag{63}$$

$$b_1 = -\dot{\phi}_r^2 mrl\sin\phi_r - mgl\sin\phi_r + D_\phi\dot{\phi}_r \tag{64}$$

$$b_2 = \dot{\phi}_r^2 mrl\sin\phi_r + D_\theta\dot{\theta}_r \tag{65}$$

TABLE VI
PARAMETERS OF THE AXIAL TORQUE SENSOR (CFS080CS102A)

Explanation	Value	Unit
Power supply voltage	5	V
Dimensions	80	mm
Rated load Fx,Fy,Fz	1000	N
Rated load Mx,My,Mz	30	Nm
Interface RS422	460800	bps

The torque applied to the robotic cane is calculated from the measured force F_x along the x-axis and the torque M_x on the y-axis as follows:

$$d = F_x l_x + M_y \tag{66}$$

where l_x is the distance along the x-axis from the force sensor CFS080CS102A (Table VI) to the motor axis, and M_y is demonstrated in Fig. 7.

As an example, the disturbance along the x-axis was compared with that estimated by (49) on the x axis for example.

This article has been accepted for publication in a future issue of this journal, but has not been fully edited. Content may change prior to final publication. Citation information: DOI 10.1109/TII.2019.2903893, IEEE Transactions on Industrial Informatics

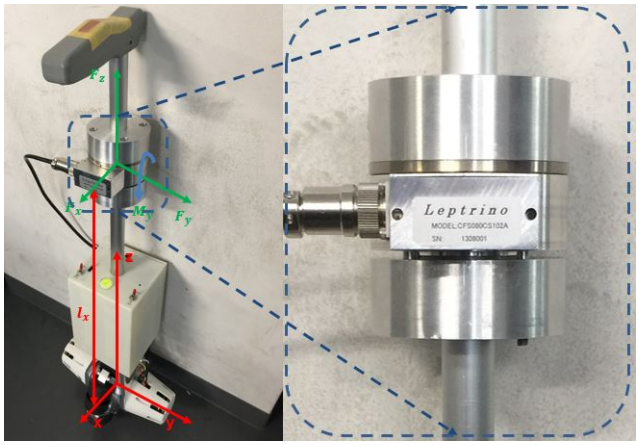

Fig. 7. Force sensor attached to the rod of the robotic cane.

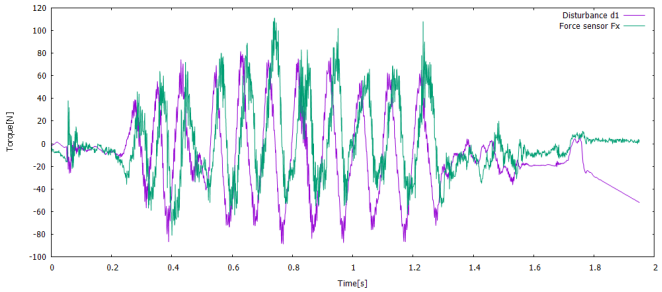

Fig. 8. Comparison of estimated (purple) and measured (green) nonlinear disturbances along the x-axis.

The results are plotted in Fig. 8. The force estimated by the nonlinear disturbance observer almost matched the force measured by the force sensor over the whole period, confirming the proper working of the designed nonlinear disturbance observer.

D. Controller of the robotic cane

Figure 9 shows the structure of the controller governed by the above equations. The coordinate transformation equations determine the current state of the robotic cane. From these coordinate transformation equations, the nonlinear disturbance observer calculates the reference signal of the robotic cane.

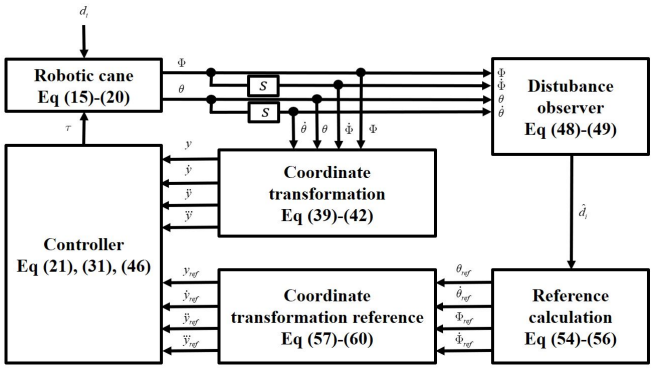

Fig. 9. Structure of the controller for the robotic cane to assist users in maintaining balance.

IV. Simulation and Experimental Results

The hardware of the robotic cane and its controller were designed in the previous section. This section presents experimental and simulation results. The measured parameters of the system are given in Table VII.

TABLE VII
MEASURED PARAMETERS OF THE ROBOTIC CANE

Symbol	Sagittal plane	Lateral plane	Unit
T_s	1e-4	1e-4	s
D_ϕ	0.01	0.02	N.m.s/rad
D_θ	0.01	0.02	N.m.s/rad
l	0.45	0.50	m
m	6.66	9.0	kg
M	2.60	0.26	kg
g	9.81	9.81	m/s^2
r	0.1	0.025	m

To ensure the safety of the robotic cane during use, we propose the following specifications of the controller:

- The cane angle at which the robotic cane supports balance maintenance ranges from -0.5 rad to $+0.5$ rad.
- The best working range of the cane angle is -0.25 rad to $+0.25$ rad.
- The feedback speed of the robotic cane responding to the behavior of the users ranges from -0.3 m/s to $+0.3$ m/s. This speed is limited by special needs of elderly users.

In 3-D simulations and experiments, we first consider the stability of the robotic cane without human support. We then consider the response of the robotic cane when supporting the balance maintenance of real users.

A. Simulation results

A 3-D model of the robotic cane was programmed in the C/C++ language. The simulation results based on LAM and the nonlinear disturbance observer were stable around the equilibrium position (see Fig. 10).

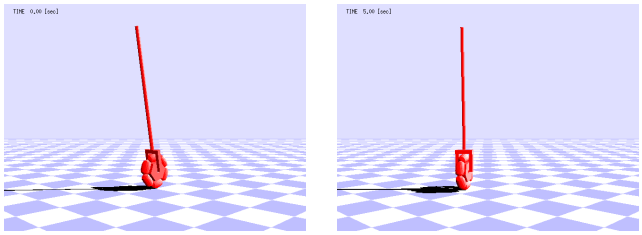

a) b)

Fig. 10. Stabilization of the robotic cane around the balance point in a 3D simulation: (a) starting point at 0.17 rad; (b) position after 5 s.

As shown in Figs. 10-11, the robotic cane was initially angled at 0.17 rad. After reaching the zero point (0.0 rad), it remained balanced around the zero point (Fig. 11 (a) with very small fluctuations around the equilibrium position (Fig. 11 (b)).

Specifically, from a starting angle of 0.17 rad, the robotic cane reached the equilibrium point (0.0 rad) after 0.3 s. Thereafter, it slightly fluctuated by ± 0.005 rad before properly stabilizing (Fig. 11 (a)).

This article has been accepted for publication in a future issue of this journal, but has not been fully edited. Content may change prior to final publication. Citation information: DOI 10.1109/TII.2019.2903893, IEEE Transactions on Industrial Informatics

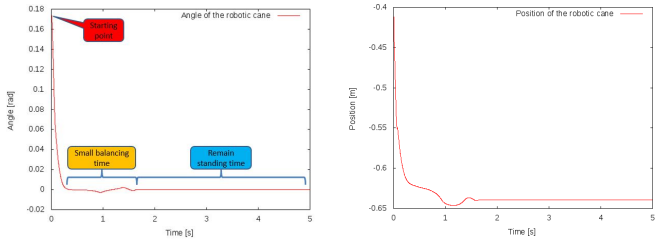

a) b)

Fig. 11. Angle and position on the sagittal plane of the robotic cane: (a) Angle; (b) Position.

The position of the robotic cane changed more rapidly than the angle (from approximately -0.42 m to -0.62 m during the same initial period), then varied slightly before stabilizing at -0.63 m (Fig. 11 (b)).

B. Comparison of the performances of LAM and LQR

Some researchers [24], [25] have stabilized the nonlinear system for the inverted pendulum using the LQR method. However, LQR can only linearize around the zero point, whereas the robotic cane must operate over a wide range of rod angles.

In the present controller design, we apply the LQR method with the simple approximation $\phi = 0$ giving $\sin\phi = \phi$, $\cos\phi = 1$, and $\dot{\phi}^2\phi = 0$.

Assuming also an infinite time horizon, the linearization quadratic regulator cost function is defined as (67):

$$J(u) = \int_0^\infty (x^T Q x + u^T R u) dt \tag{67}$$

The optimal control is given by (68), where K is the steady-state feedback gain of the controller:

$$u(t) = -Kx(t) \tag{68}$$

The robotic cane angles determined by LAM and LQR method are compared in Fig. 12. The LAM results show higher stability performance than the traditional LQR results. Especially from 25 s to the end of the period, the robotic cane based on the LQR method was unstable, fluctuating between -0.03 rad and 0.03 rad. During this time, the robotic cane based on the proposed LAM remained at nearly 0 rad.

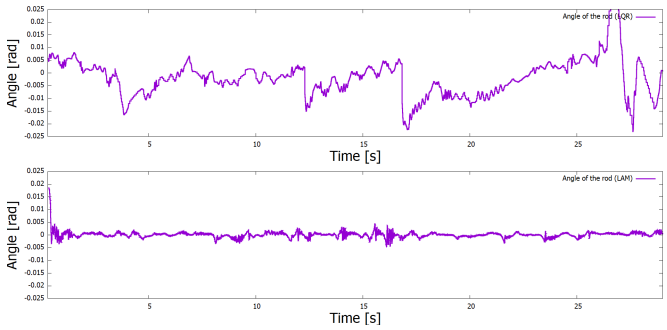

Fig. 12. Angle of the robotic cane on the sagittal plane, calculated by the LQR method (top) and LAM (bottom).

The superior performance of LAM over LQR is consolidated by the positions of the robotic cane in the two methods (see Fig. 13). In the LAM-based method, the robotic cane self-stabilized around 0 rad with no further movements, whereas in the LQR-based method, it shifted between -0.05 m and 0.05 m during the first period, becoming unstable after 25 s.

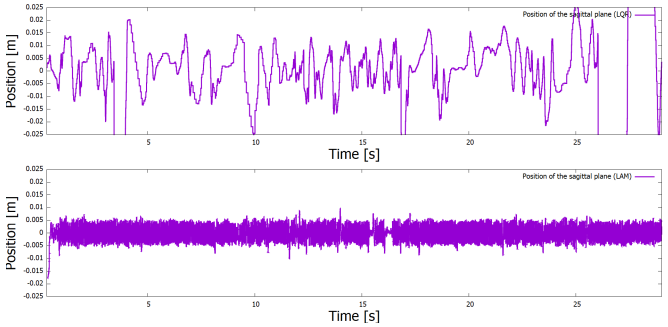

Fig. 13. Position of the robotic cane on the sagittal plane, calculated by the LQR method (top) and LAM (bottom).

C. Experimental results of the hardware controller of the robotic cane

This subsection tests the control algorithm of the robotic cane. The robotic cane is various balance situations is photographed in Fig. 14.

a) b) c) d)

Fig. 14. Stabilization of the robotic cane around its balancing point: (a) Without the external battery, (b) with the external battery, (c) supporting the user while standing and (d) supporting walking in the sagittal plane.

As shown in Figure 14 (a), the robotic cane balanced around its equilibrium point when powered by the internal battery. In this situation, it can operate for 30 minutes before the battery needs charging.

Figure 14 (b) shows the robotic cane equipped with the outer battery, which extends the operating time to more then 2 hours.

In both planes, the angle of the stabilized robotic cane changed very slightly around the balance point of the cane (± 0.01 rad in the sagittal plane, and only -0.006 to 0.001 rad in the lateral plane, from starting angles of -0.32 rad and -0.12 rad, respectively). The angle fluctuations in both planes are plotted in Figure 15.

As shown in Figure 16, the position of the robotic cane was almost completely stable around the equilibrium point. The position showed very small fluctuations around the zero points (maximum range 1 cm) in the lateral plane, and varied

This article has been accepted for publication in a future issue of this journal, but has not been fully edited. Content may change prior to final publication. Citation information: DOI 10.1109/TII.2019.2903893, IEEE Transactions on Industrial Informatics

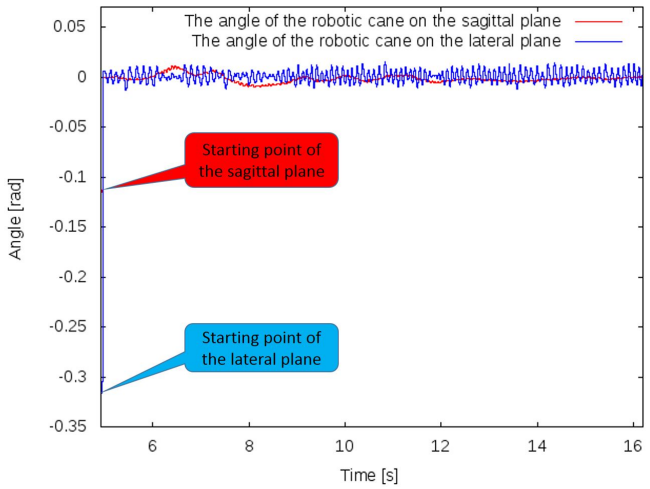

Fig. 15. Angles around the balancing point of the robotic cane in the lateral (blue) and sagittal (red) planes.

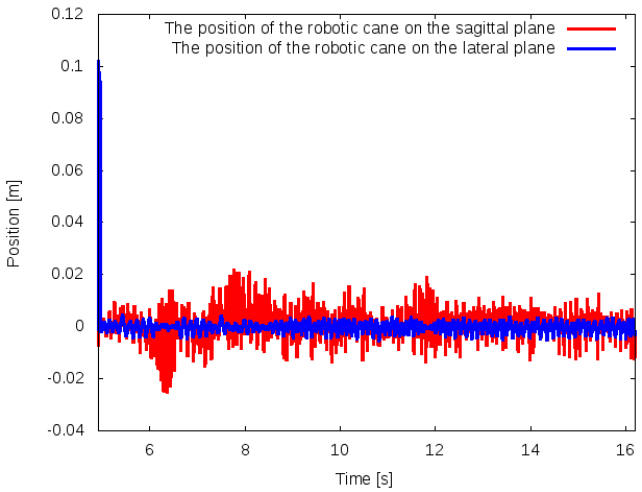

Fig. 16. Positions of the robotic cane when stabilized around its balancing point in the lateral (blue) and sagittal (red) planes.

by ± 0.01 m in the sagittal plane. These results show that LAM combined with the nonlinear disturbance observer enables long-time balancing of the robotic cane around its equilibrium position with no external support.

Next, we tested whether the robotic cane can support the balance of users (panels (c) and (d) of Fig. 14). The user is supported by grasping the handle of the robotic cane when the cane has stabilized around its equilibrium point (Fig. 14 (c)). When the angle of the robotic cane changes under s small applied force, the cane moves alongside the user, maintaining the user's balance throughout the walking motion (Fig. 14 (d)).

From a starting angle of 0.025 rad, the robotic cane obtained the balance point at 2 seconds. Thereafter, it assisted the standing user from 2 to 20 s with small fluctuations around 0 rad Figure 17.

When the user began walking (at $20 - 25$ s), the angle changed under the application of a small force, and the robotic cane moved simultaneously with the user.

In the next experiment, the balance of an unsteady user was

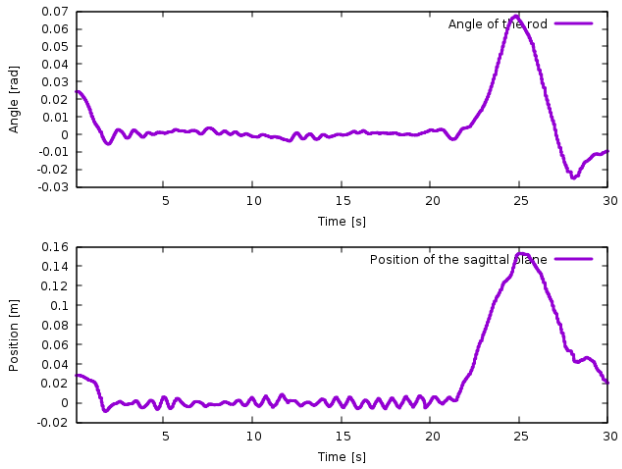

Fig. 17. Angle (top) and position (bottom) of the robotic cane when helping the user to stand (2-20) s and walk (20-30) s.

assisted by the cane moving alongside the user. The angle and position of the robotic cane in this experiment are plotted in Figure 18.

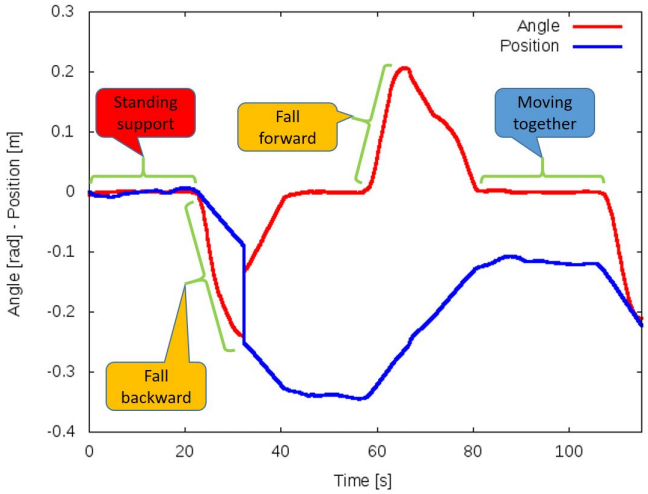

Fig. 18. Position and sagittal angle of robotic cane when helping the user to move while beginning to fall backward or forward.

As shown in Fig. 19 (a zoom in of Fig. 18), the angle of the robotic cane fluctuated by only ± 0.0015 rad between 2.5 and 22 s, when the cane was offering standing support.

When the user began falling backward (Fig. 20 (a)) the robotic cane moved quickly to the standing state with a small positional vibration, returning the user to the equilibrium point (see Fig. 20 (b)).

During this time ($22 - 35$ s), the robotic cane immediately responded to the angle change, establishing the new position of the balancing point (Fig. 18).

Similarly, when the user began fall forward (Fig. 20 (c)), the robotic cane changed its position to support the user's standing motion (Fig. 20 (d)). The angle feedback position of the robotic cane are shown in the $60 - 80$ s period of Fig. 18.

In the self-balanced state, the robotic cane slightly vibrated around the equilibrium position (1 - 13 s in Fig. 21). This

This article has been accepted for publication in a future issue of this journal, but has not been fully edited. Content may change prior to final publication. Citation information: DOI 10.1109/TII.2019.2903893, IEEE Transactions on Industrial Informatics

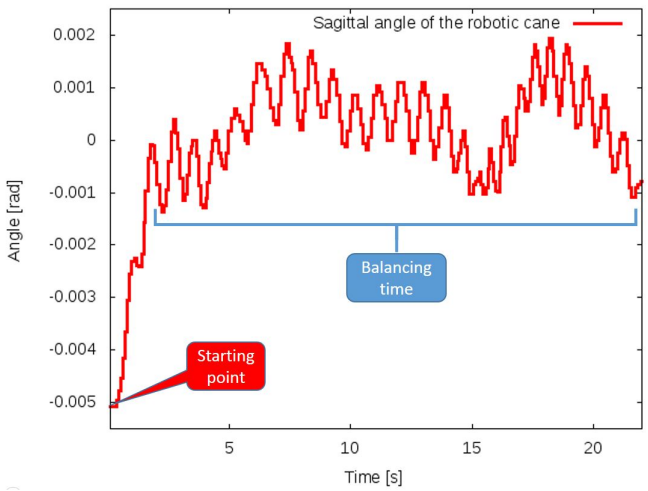

Fig. 19. Angle of the robotic cane between 2.5 and 22 s (zoom in of Fig. 18).

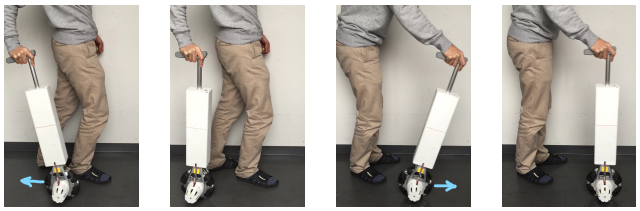

Fig. 20. Robotic cane helping the user to maintain balance at the start of falling: (a) user begins to fall backward, (b) the robotic cane changes its location to restore the user's balance, (c) user begins to fall forward, (d) the robotic cane again changes its location to restore the user's balance.

vibration is attributable to the design error of the gearbox and the high-gain controller.

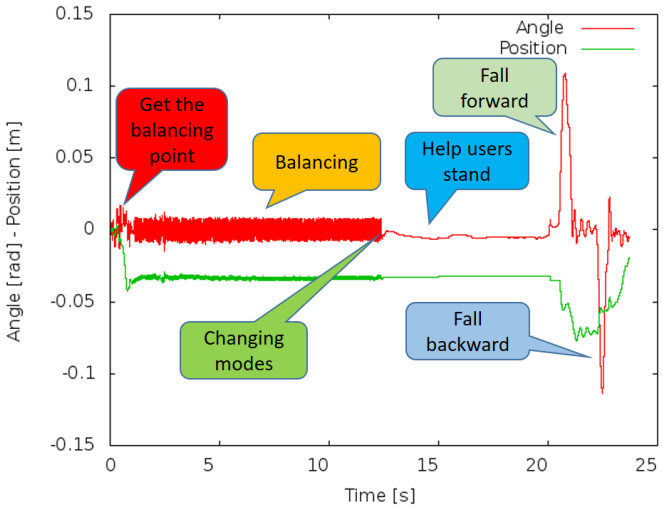

Fig. 21. Balance assistance by the robotic cane. The touch sensor changes the stability mode from self-stability to user support.

To suppress this vibration, we mounted a touch sensor on top of the handle (see Fig. 1). When the user grasped the handle with the touch sensor, the vibration was completely suppressed (after 13 s in Fig. 21), and the robotic cane switched to the assistance mode.

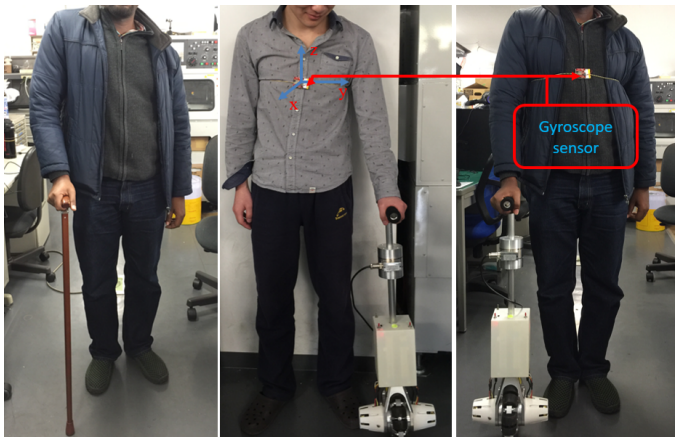

Fig. 22. Gyroscope sensor mounted on the body of a user supported by a traditional cane (left) and the robotic cane (center and right).

Table VIII shows the vibration magnitudes of the user's body measured by the gyroscope sensor in three user states: without support, supported by a traditional cane, and supported by the robotic cane. The measurements were made on seven subjects (Fig. 22).

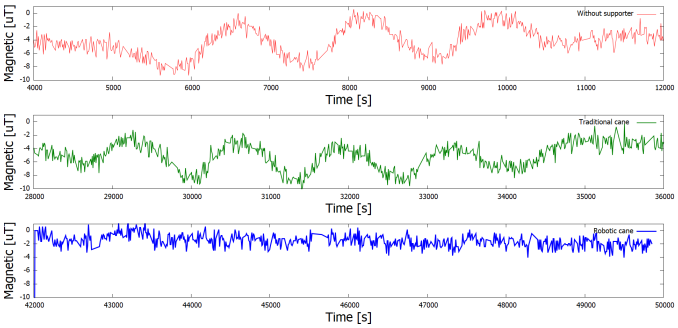

Fig. 23. Body vibrations in the lateral plane of users walking with no support (top), a traditional cane (center), and the robotic cane (bottom).

As shown in the top panel of Fig. 23, the body vibrations were largest when the subject walked without a support device (ranging from -10 to 0 μT) and the subject expended the largest energy in walking. To reduce this vibration, the subject used the traditional cane for walking assistance, but the vibration amplitude still fluctuated between -9 and 0 μT when the cane was lifted from the ground (center panel of Fig. 23). At that time, the user received no support from the walking aid. In contrast, the robotic cane attenuated the user's vibrations to a small range (-4 to 1 μT) and largely reduced the energy of walking (bottom panel of Fig. 23).

The results of the other subjects are also given in Table VIII. The robotic cane reduced the body vibrations in the no support and traditional cane cases by 3.12 times and 2.48 times, respectively.

Moreover, as confirmed in Table VIII, the balance-support performance of the controller and nonlinear disturbance observer in the robotic cane is almost independent of user age.

This article has been accepted for publication in a future issue of this journal, but has not been fully edited. Content may change prior to final publication. Citation information: DOI 10.1109/TII.2019.2903893, IEEE Transactions on Industrial Informatics

TABLE VIII
BODY VIBRATIONS IN THE LATERAL PLANE OF SEVEN SUBJECTS USING NO AID, A TRADITIONAL CANE, AND THE PROPOSED ROBOTIC CANE

Subjects	Without supporter (μT)		Traditional cane (μT)		Robotic cane (μT)	
	Min	Max	Min	Max	Min	Max
1	-10	0	-9	0	-4	-1
2	32	41	20	28	22	26
3	-24	-10	-25	-17	-16	-13
4	-21	-9	-12	-2	-5	-8
5	12	29	11	20	13	18
6	29	35	30	35	32	34
7	2	12	5	11	4	7
Average	11.14		8.86		3.57	

Subjects	Gender	Age[Years]	Weight[Kg]	Height[m]
1	Male	28	55	1.68
2	Male	30	62	1.72
3	Male	25	56	1.62
4	Male	27	53	1.70
5	Male	32	58	1.75
6	Male	31	68	1.67
7	Male	26	60	1.60

The ratchet structure shown in Fig. 24 rotates and maintains the robot's state at any position, guaranteeing strong and immediate support by the robotic cane.

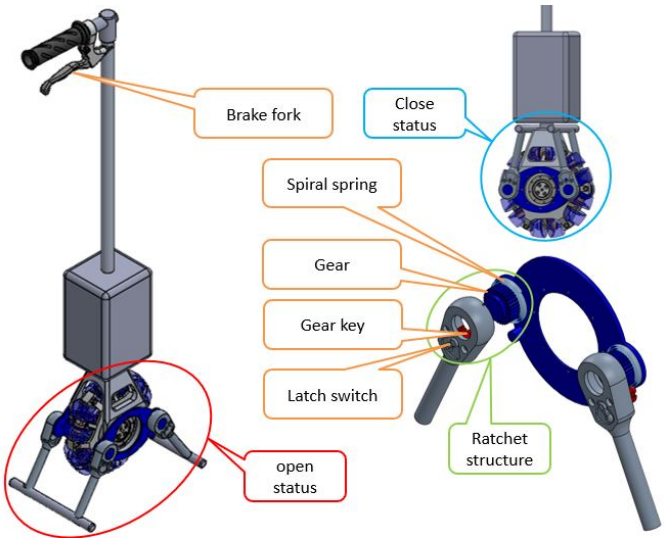

Fig. 24. Structure of the ratchet frame stand support.

By using a gear key and a latch switch, the ratchet structure rotates in only one direction. The angular direction depends on the latch-switch status, and the ratchet structure is rapidly opened by releasing a spiral spring when the brake fork is activated by the user. This structure maintains a stronger status of the frame the present state than other structures.

When the user begins falling backward or forward, the brake fork on the grip handle immediately opens the ratchet structure and the closed state (Fig. 25 (a)) converts to the open state for stable user support (Fig. 25 (b)).

V. CONCLUSIONS

We designed and fabricated the hardware of a robotic cane with an omnidirectional wheel and a high speed processing

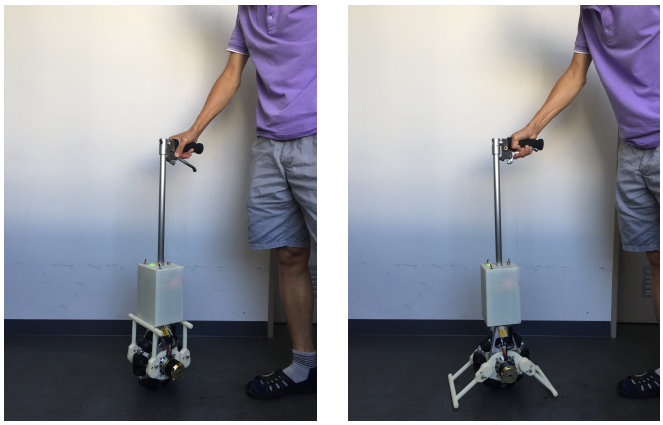

a) b)

Fig. 25. Ratchet frame status when a robotic cane support the user maintain balancing: (a) Before open; (b) After open.

controller for assisted standing and walking. The controller estimates the user's external force by a LAM-based linearization system with a nonlinear disturbance observer. In 3D simulations and physical tests of the robotic cane hardware, the robotic cane provided better balance maintenance support than previously proposed methods. The proposed robotic cane proved an excellent candidate in various assistance modes: self-balancing, standing assistance, walking assistance, fall prevention, and a mechatronic safety mode.

In future work, we will reduce the size of the robotic cane and increase the working time of the batteries before recharging is required. To lessen the weight and cost of the robotic cane, we will also investigate a new motor driver for the brushless motors. We will then test a commercial version of the robotic cane in rehabilitation centers and hospitals.

REFERENCES

[1] R. Suzman and J. Beard. Global health and aging. [Online]. Available: http://www.who.int/ageing/publications/global_health.pdf

[2] T. Kagawa, H. Ishikawa, T. Kato, C. Sung, and Y. Uno, "Optimization-based motion planning in joint space for walking assistance with wearable robot," *IEEE Transactions on Robotics*, vol. 31, DOI 10.1109/TRO.2015.2409434, no. 2, pp. 415–424, Apr. 2015.

[3] S. Hauser, M. Robertson, A. Ijspeert, and J. Paik, "Jammjoint a variable stiffness device based on granular jamming for wearable joint support," *IEEE Robotics and Automation Letters*, vol. 2, DOI 10.1109/LRA.2017.2655109, no. 2, pp. 849–855, Apr. 2017.

[4] S. Y. Kim, L. Yang, I. J. Park, E. J. Kim, M. S. Park, S. H. You, Y. H. Kim, H. Y. Ko, and Y. I. Shin, "Effects of innovative walkbot robotic-assisted locomotor training on balance and gait recovery in hemiparetic stroke: A prospective, randomized, experimenter blinded case control study with a four-week follow-up," *IEEE Transactions on Industrial Electronics*, vol. 23, DOI 10.1109/TNSRE.2015.2404936, no. 4, pp. 636–642, Jul. 2015.

[5] B. Koopman, E. H. F. van Asseldonk, and H. van der Kooij, "Estimation of human hip and knee multi joint dynamics using the lopes gait trainer," *IEEE Transactions on Robotics*, vol. 32, DOI 10.1109/TRO.2016.2572695, no. 4, pp. 920–932, Aug. 2016.

[6] H. Lee and N. Hogan, "Time varying ankle mechanical impedance during human locomotion," *IEEE Transactions on Neural Systems and Rehabilitation Engineering*, vol. 23, DOI 10.1109/TNSRE.2014.2346927, no. 5, pp. 755–764, Sep. 2015.

[7] J. Li, B. Shen, C. M. Chew, C. L. Teo, and A. N. Poo, "Novel functional task based gait assistance control of lower extremity assistive device for level walking," *IEEE Transactions on Industrial Electronics*, vol. 63, DOI 10.1109/TIE.2015.2477347, no. 2, pp. 1096–1106, Feb. 2016.

[8] H. Yu, S. Huang, G. Chen, Y. Pan, and Z. Guo, "Human robot interaction control of rehabilitation robots with series elastic actuators," *IEEE Transactions on Robotics*, vol. 31, DOI 10.1109/TRO.2015.2457314, no. 5, pp. 1089–1100, Oct. 2015.

[9] D. Zanotto, Y. Akiyama, P. Stegall, and S. K. Agrawal, "Knee joint misalignment in exoskeletons for the lower extremities effects on user's gait," *IEEE Transactions on Robotics*, vol. 31, DOI 10.1109/TRO.2015.2450414, no. 4, pp. 978–987, Aug. 2015.

[10] C. Zhu, M. Oda, M. Suzuki, X. Luo, H. Watanabe, and Y. Yan, "A new type of omnidirectional wheelchair robot for walking support and power assistance," *2010 IEEE International Conference on Intelligent Robots and Systems*, DOI 10.1109/IROS.2010.5652805, pp. 6028–6033, Oct. 2010.

[11] G. Jang, J. Kim, S. Lee, and Y. Choi, "Emg based continuous control scheme with simple classifier for electric powered wheelchair," *IEEE Transactions on Industrial Electronics*, vol. 63, DOI 10.1109/TIE.2016.2522385, no. 6, pp. 3695–3705, Jun. 2016.

[12] Y. H. Hsieh, K. Y. Young, and C. H. Ko, "Effective maneuver for passive robot walking helper based on user intention," *IEEE Transactions on Industrial Electronics*, vol. 62, DOI 10.1109/TIE.2015.2416679, no. 10, pp. 6404–6416, Oct. 2015.

[13] C. D. Lim, C. M. Wang, C. Y. Cheng, Y. Chao, S. H. Tseng, and L. C. Fu, "Sensory cues guided rehabilitation robotic walker realized by depth image - based gait analysis," *IEEE Transactions on Automation Science and Engineering*, vol. 13, DOI 10.1109/TASE.2015.2494067, no. 1, pp. 171–180, Jan. 2016.

[14] S. Nakagawa, Y. Hasegawa, T. Fukuda, I. Kondo, M. Tanimoto, P. Di, J. Huang, and Q. Huang, "Tandem stance avoidance using adaptive and asymmetric admittance control for fall prevention," *IEEE Transactions on Neural Systems and Rehabilitation Engineering*, vol. 24, DOI 10.1109/TNSRE.2015.2429315, no. 5, pp. 542–550, May. 2016.

[15] K. Shimizu and Y. Fujimoto, "A robotic cane for walking support using two control modes," in *IEEJ International Workshop on Sensing, Actuation, Motion Control, and Optimization*, pp. TT9–5, Mar. 2016.

[16] K. Shimizu, S. A. Issam, and Y. Fujimoto, "Operation verification of cane type walking support robot in step and slope situation," in *IEEJ International Workshop on Sensing, Actuation, Motion Control, and Optimization*, Mar. 2015.

[17] K. Shimizu, S. A. Issam, and Y. Fujimoto, "Examination of a control method for a walking assistance robotics cane," in *IEEE Industrial Electronics Society Annual Conference (IECON)*, DOI 10.1109/IECON.2014.7048899, pp. 1968–1973, Oct. 2014.

[18] K. Shimizu, S. A. Issam, and Y. Fujimoto, "A robotic cane for walking assistance'," in *IEEJ International Power Electronics Conference (IPEC)*, DOI 10.1109/IPEC.2014.6869857, pp. 1968–1973, May. 2014.

[19] Y. Ota, M. Ryumae, and K. Sato, "Robotic cane devices," *United States Patent Application Publication*, no. US 2013/0041507 A1, 2013.

[20] D. Yang, E. Sihite, J. M. Friesen, and T. Bewley, "Design and control of a micro ball-balancing robot (mbbr) with orthogonal midlatitude omniwheel placement," *IEEE/RSJ International Conference on Intelligent Robots and Systems (IROS)*, Sep. 2016.

[21] C. S. Chen and W. L. Chen, "Robust adaptive sliding mode control using fuzzy modeling for an inverted pendulum system," *IEEE Transactions on Industrial Electronics*, vol. 45, DOI 10.1109/41.681229, no. 2, pp. 297–306, Apr. 1998.

[22] M. J. Mahmoodabadi and S. A. Mostaghim, "Stability of nonlinear systems using optimal fuzzy controllers and its simulation by java programming," *IEEE Journal of Automatica Sinica*, vol. pp, DOI 10.1109/JAS.2017.7510388, no. 99, pp. 1–10, Jan. 2017.

[23] L. S. Qin, J. J. Hu, H. X. Li, and W. Chen, "Fuzzy logic controllers for specialty vehicles using a combination of phase plane analysis and variable universe approach," *IEEE Access*, vol. 5, DOI 10.1109/ACCESS.2017.2656124, no. 99, pp. 1579–1588, Jan. 2017.

[24] P. V. Lam and Y. Fujimoto, "Completed hardware design and controller of the robotic cane using the inverted pendulum for walking assistance," *2017 IEEE 26th International Symposium on Industrial Electronics (ISIE)*, vol. 19-21 June 2017, DOI 10.1109/ISIE.2017.8001547, pp. 2163–5145, Aug. 2017.

[25] P. V. Lam and Y. Fujimoto, "Building and test a controller of the robotic cane for walking assistance," in *The IEEJ International Workshop on Sensing, Actuation, Motion Control, and Optimization*, vol. 3, pp. SS2–6, Mar. 2017.

[26] P. Shi, H. Wang, and C. C. Lim, "Network based event triggered control for singular systems with quantizations," *IEEE Transactions on Industrial Electronics*, vol. 63, DOI 10.1109/TIE.2015.2475515, no. 2, pp. 1230–1238, Feb. 2016.

[27] L. M. L. Orozco, G. R. Lomeli, J. G. R. Moreno, and M. T. Perea, "Identification inverted pendulum system using multilayer and polynomial neural networks," *IEEE Latin America Transactions*, vol. 13, DOI 10.1109/TLA.2015.7112017, no. 5, pp. 1569–1576, May. 2015.

[28] J. Huang, Z. H. Guan, T. Matsuno, T. Fukuda, and K. Sekiyama, "Sliding mode velocity control of mobile wheeled inverted pendulum systems," *IEEE Transactions on Robotics*, vol. 26, DOI 10.1109/TRO.2010.2053732, no. 4, pp. 750–758, Aug. 2010.

[29] H. Fukushima, K. Muro, and F. Matsuno, "Sliding mode control for transformation to an inverted pendulum mode of a mobile robot with wheel arms," *IEEE Transactions on Industrial Electronics*, vol. 62, DOI 10.1109/TIE.2014.2384475, no. 7, pp. 4257–4266, Jul. 2015.

[30] J. Huang, S. Ri, L. Liu, Y. Wang, J. Kim, and G. Pak, "Nonlinear disturbance observer based dynamic surface control of mobile wheeled inverted pendulum," *IEEE Transactions on Control Systems Technology*, vol. 23, DOI 10.1109/TCST.2015.2404897, no. 6, pp. 2400–2407, Nov. 2015.

[31] S. K. A. Kaustubh Pathak, JaumeFranch, "Velocity and position control of a wheeled inverted pendulum by partial feedback linearization," *IEEE Transactions on Robotics*, vol. 21, no. 3, Jun. 2005.

[32] S. A. H. N. R. Gans, "Visual servo velocity and pose control of a wheeled inverted pendulum through partial feedback linearization," *IEEE International Conference on Intelligent Robots and Systems*, Oct. 2006.

[33] J. B. M. Hari Vasudevan, Aaron M. Dollar, "Design for control of wheeled inverted pendulum platforms," *Journal of Mechanisms and Robotics*, DOI 10.1115/1.4029401, 2015.

[34] A. Isidori, "Nonlinear control systems: An introduction," in *Third edition, Chapter 4, London, UK: Springer-Verlag*, 2001.